A data-driven modeling approach to quantify morphology effects on transport properties in nanostructured NMC particles

Matthias Neumann[a,*], Sven E. Wetterauer[b], Markus Osenberg[c], André Hilger[c], Phillip Gräfensteiner[a], Amalia Wagner[d], Nicole Bohn[d], Joachim R. Binder[d], Ingo Manke[c], Thomas Carraro[e], Volker Schmidt[a]

[a]*Institute of Stochastics, Ulm University, Helmholtzstraße 18, 89069 Ulm, Germany*
[b]*Institute for Applied Mathematics, Heidelberg University, Im Neuenheimer Feld 205, 69120 Heidelberg, Germany*
[c]*Institute of Applied Materials, Helmholtz-Zentrum Berlin für Materialien und Energie, Hahn-Meitner-Platz 1, 14109 Berlin, Germany*
[d]*Institute for Applied Materials, Karlsruhe Institute of Technology, Hermann-von-Helmholtz-Platz 1, 76344 Eggenstein-Leopoldshafen, Germany*
[e]*Chair of Applied Mathematics, Helmut Schmidt University / University of the Federal Armed Forces Hamburg, Holstenhofweg 85, 22043 Hamburg, Germany*

Abstract

We present a data-driven modeling approach to quantify morphology effects on transport properties in nanostructured materials. Our approach is based on the combination of stochastic modeling of the 3D nanostructure and numerical modeling of effective transport properties, which is used to investigate process-structure-property relationships of hierarchically structured cathode materials for lithium-ion batteries. We focus on nanostructured $LiNi_{1/3}Mn_{1/3}Co_{1/3}O_2$ (NMC) particles, the nanoporous morphology of which has a crucial impact on their effective transport properties (*i.e.*, effective ionic and electric conductivity) and thus on the performance of the cell. First, we develop a parametric stochastic model for the 3D morphology of the nanostructured NMC particles based on excursion sets of so-called χ^2-fields. This model, which has only two parameters, is then fitted to FIB-SEM image data of the NMC particles manufactured with different calcination temperatures and different particle sizes. This way it is possible to generate digital twins of the NMC particles. In a second step, measured 3D image data and corresponding digital twins are used as input for the numerical simulation of effective transport properties. Based on the results obtained by these simulations, we can quantify process-structure-property relationships. Overall, we present a methodological framework that allows for an efficient optimization of the fabrication process of nanostructured NMC particles.

*Corresponding author.

Keywords: Digital twin, effective tortuosity, FIB-SEM tomography, finite element modeling, nanostructured battery material, stochastic 3D modeling, transport in porous media

1. Introduction

Energy storage is one of the most important issues with regard to the decarbonization of the power sector [1]. This leads, in particular, to an increasing need for the development of efficient new battery systems and the further optimization of existing systems. One promising approach to further improve the performance of cathodes is the use of hierarchically structured active materials, as proposed in [2] for lithium-ion batteries and in [3] for sodium-ion batteries. In [4, 5], a detailed study of cathodes with nanostructured $LiNi_{1/3}Mn_{1/3}Co_{1/3}O_2$ (NMC) particles as active material is presented, where differently prepared active material particles are considered, varying both, the size of the particles forming the aggregated nanoporous active material particles and the calcination temperature to synthesize the aggregated particles. Based on 3D image data, the influence of fabrication parameters on descriptors of the morphology and performance of cathodes, such as the experimentally determined specific capacity, is quantified. Note that the 3D morphology of cathodes is investigated on two different length scales, namely the arrangement of the active material in the electrode (at the micrometer scale) and the morphology of the nanoporous active material particles (at the nanometer scale).

Since 3D imaging is costly and time consuming, only a small number of tomographically measured samples can be studied. Thus, to quantitatively investigate process-structure-property relationships based on a few datasets of measured 3D images, a common approach is to develop mathematical tools for the generation of model-based digital twins of micro- or nanostructures observed by 3D imaging. For this purpose, stochastic modeling of 3D morphologies [6–8] is combined with numerical modeling of effective transport properties [9], it is possible to study process-structure-property relationships based on modeling and simulation. Note that, in this context, we follow [10] defining digital twins as "a high-fidelity in-silico representation closely mirroring the form (i.e., appearance) and the functional response of a specified (unique) physical twin". The physical twin, i.e., the micro- or nanostructure under consideration, is first represented as a 3D image. Second, the calibration of a parametric stochastic model to image data builds the bridge between reality and the virtual space, since it allows for the simulation of structures which are statistically mirroring the appearance of the physical structure. Finally, model validation regarding the functional response, which is

given by effective transport properties in this case, has to be performed to ensure that the model creates digital twins.

Using methods of stochastic geometry, 3D models have been developed to generate digital twins of battery materials at the micro-scale, *i.e.*, for the arrangement of active material particles in the electrode [11–13]. Furthermore, on micro- and nano-scales, such modeling techniques have been used to generate digital twins of the outer shell and inner polycrystaline grain architecture of cathode particles for Li-ion batteries [14]. On both scales, the corresponding models have been fitted to tomographic image data. Moreover, machine learning approaches have recently been used for the data-driven generation of digital twins of complex 3D morphologies, see [15–17]. However, to the best of our knowledge, there are no stochastic models available in the literature, which allow us to statistically reproduce the 3D morphology of nanostructured active material particles as digital twins. Filling this gap is the main aim of the present paper, where our modeling approach is based on excursion sets of random fields, see e.g. Section 6.6.3 of [6]. Note that this concept has been successfully applied to model the 3D morphology of anode materials in lithium-ion batteries [18] as well as of (three-phase) anode materials in solid oxide fuel cells [19–22] and gas-diffusion electrodes [23]. In the latter cases, excursion sets of Gaussian random fields have been used as modeling tool.

In the present paper, we consider so-called χ^2-random fields, like in [18], where we derive a new analytical formula for the two-point coverage probability function that allows for an efficient model calibration to image data. In particular, model calibration is performed on the basis of 3D image data obtained by FIB-SEM tomography [24, 25], which represents the 3D morphology of (differently manufactured) nanostructured NMC particles utilized already in [5]. The goodness of model fit is validated with respect to both, geometrical descriptors as well as effective transport properties of samples of virtual NMC particles drawn from the fitted particle model.

Note that effective transport properties of porous media are usually determined by finite element modeling (FEM), which is extensively used in the literature to investigate structure-property relationships of electrode materials in fuel cells and batteries, see Section 3.2.1 of [26] and the references therein. In the present paper, to compute effective transport properties via FEM, the solid phase of simulated NMC particles is represented as a union of sub-particles. Each of these sub-particles is analytically described by spherical harmonics [27, 28], see also [29], where spherical harmonics have been used to describe the outer shape of active material particles in electrodes of Li-ion batteries. This way we get an analytical

representation of the solid phase of nanostructured active material particles, which is used as geometry input for FEM.

Altogether, we develop a data-driven framework to investigate process-structure-property relationships. In particular, we show that regression formulas like those empirically derived in [30–33] are appropriate to quantify the impact of 3D morphology on effective conductivity and effective diffusivity in the solid phase and pore space, respectively, of nanostructured NMC particles. Furthermore, the obtained results of effective transport properties can then be used as homogenized input for simulations on the electrode scale. Note that the computation of effective transport coefficients is required in multiscale approaches to model and simulate electrochemical processes on the macro-scale of the electrodes. A direct computation on the nano-scale, especially for hierarchically structured electrodes, would not be computationally feasible in practice. Thus, the present paper supports in-depth studies on upscaling from the nano- to the macro-scale and, in this way, it contributes to a better understanding of process-structure-property relationships for hierarchically structured battery electrodes through modeling and simulation, which is crucial for further optimizing such materials.

The rest of this paper is organized as follows. The materials under consideration and the acquisition of 3D image data is described in Section 2. The spatial stochastic model, which has been developed for the 3D morphology of nanostructured NMC particles as well as the structural segmentation of both, measured and simulated image data, are presented in Section 3. This structural segmentation serves as geometry input for the numerical transport simulations described in Section 4. Process-structure-property relationships are discussed in Section 5. Section 6 concludes.

2. Materials and Imaging

2.1. Preparation of hierarchically structured active material

The preparation of hierarchically structured NMC111 active material with three different secondary particle sizes and varying nanostructure was performed by grinding, spray drying and calcination. Therefore, NMC111 (Toda Kogyo Corp.) was ground in deionized water with Darvan 821A dispersant (Vanderbilt Minerals) for around 5 h in an agitator bead mill (LabStar LS1, Netzsch) with yttria-stabilized zirconia beads (diameter: 0.2 mm) at 3000 rpm. The grinding process was stopped at a mean particle size (considering the volume-weighted median $d_{50,3}$) of approximately 220 nm. Subsequently PEG400 (Sigma Aldrich) was added as dispersant, mixed thoroughly and the suspensions was divided into two fractions

of equal volumes. Spray drying was performed in a MobileMinor spray dryer from GEA at three different peripheral speeds of the atomizer wheel to obtain varying secondary particle sizes. Therefore 1 bar (12000 rpm), 2.7 bar (27000 rpm) and around 4.5 bar (39000 rpm) nitrogen gas flow was set to drive the atomizer wheel. Obtained spray-dried granules were sieved and three fractions of secondary particle sizes, namely with $d_{50,3}$-values of around 9, 14 and 37 µm were obtained. In order to obtain nanostructured powders, which are denoted as Fine (F), Medium (M) and Coarse (C) in the following, these granules were calcined at 850 and 900°C for 5 h under pressured airflow (6 l/min) at heating and cooling rates of 5 and 10 K/min. Note that due to the manufacturing process, the size of the secondary particles (F, M, and C) also influences the formation of the morphology of nanopores within the secondary particles [5]. In the present paper, we consider fine, medium and coarse secondary particles calcined at 850 and 900°C. In the following, these samples are denoted by F850, M850, C850, F900, M900, and C900.

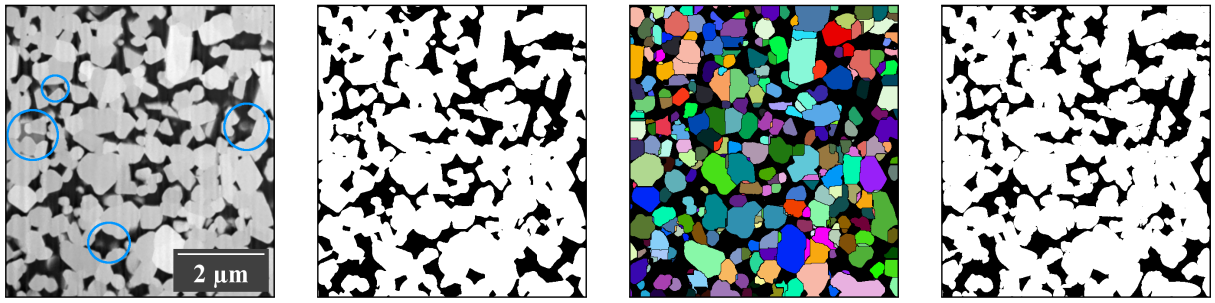

Figure 1: 2D cross-section of greyscale image obtained by FIB-SEM tomography for a nanostructured active material particle with medium particle size and a calcination temperature of 900°C , where critical regions for the segmentation are highlighted in blue (a). The greyscale image is compared with the corresponding binarized image (b), where the solid phase and the pore space are represented in white and black, respectively. Additionally, the solid phase is partitioned into sub-particles by means of the watershed algorithm (c), which is used to represent the solid phase as a union of star-shaped sets given by spherical harmonics (d).

2.2. FIB-SEM imaging

Focused ion beam-scanning electron microscopy (FIB-SEM) imaging was performed for three-dimensional structural data acquisition. The Zeiss Crossbeam 340 at the HZB Core-Lab "Correlative Microscopy and Spectroscopy" was used for each measurement. Prior to ion milling, each sample (particles in bulk) was infiltrated with resin (EpoThin 2) and polished, resulting in resin cubes containing NMC-particles with an average edge length of 1 mm. To ensure good conductivity, each cube was coated with gold (Cressington Sputter Coater 108auto, 60 seconds). On each cube, FIB-SEM tomography was performed by serial

sectioning using Ga-ions (300 pA with 30 kV) and SEM imaging (3 kV SE2 detector). For most samples, an isotropic voxel size of 10 nm was achieved, only for the sample F850°, the first sample measured in this series, a voxel size of 15 nm was reached. However, the larger voxel size had no effect on the following statistical analysis.

Due to the high contrast between the resin and NMC, the use of the automatic Otsu threshold algorithm [34] was sufficient for image segmentation, *i.e.* to classify each voxel either as pore or solid. In Figure 1, a comparison of a 2D cross-section of the greyscale image and the corresponding segmented 2D cross-section is shown for an active material particle with medium particle size and a calcination temperature of 900°C. Even if the samples are fully infiltrated with epoxy, the 3 kV SE2 detector leads to minor transparency resulting in slight shine-through artifacts. Nevertheless, the Otsu threshold provides a good segmentation, even for critical regions, a few of which are exemplarily highlighted by blue circles in Figure 1a. Moreover, note that without an infiltration of resin, more sophisticated algorithms are necessary to appropriately segment FIB-SEM images of nanoporous NMC particles [35]. Data processing was performed using the open source software ImageJ/Fiji [36].

3. Structural segmentation and stochastic 3D modeling

In Section 3.1, we first explain how the solid phase of aggregate particles can be represented by a union of sub-particles using spherical harmonics. This representation will be exploited later on for the numerical simulation of effective transport properties, see Section 4. Then, in Section 3.2, we present a spatial stochastic model, which has been developed for the 3D morphology of nanostructured NMC particles as described in Section 2. Note that the goodness of model fit is validated with respect to both, geometrical descriptors and, in Section 5, effective transport properties of samples of virtual NMC particles drawn from the fitted particle models.

3.1. Representation of solid phase by spherical harmonics

Binarized 3D image data as described in Section 2 is given on a voxel grid, *i.e.*, for each voxel the image contains the information, whether the voxel belongs to the solid phase or to the pore space of the considered aggregate particle. To obtain an off-grid representation of the nanostructure, the solid phase is represented by a union of sub-particles, which are defined in the (continuous) Euclidean space $\mathbb{R}^3$. For this purpose, we extract the sub-particles from 3D images by means of the watershed algorithm described in [37] and approximate them by series expansions with respect to spherical harmonics [27, 28]. It is important to note

that the segmentation into sub-particles is a methodological approach to obtain a lattice-free representation of the solid phase (i.e., the union of all sub-particles), rather than a perfect extraction of the real primary particles is aimed at. The benefit of an off-grid representation for the numerical simulation of effective transport properties is discussed in Section 4.2.

The representation of sub-particles by spherical harmonics leads to star-shaped sets, *i.e.*, there exists at least one point within the sub-particle such that all points of the sub-particle can be connected to this point by a straight line which is completely contained in the sub-particle. However, the star shape of sub-particles obtained in this way is far from being a restrictive model assumption. Typically, the sub-domains of binary 3D images, so-called basins, determined by a watershed algorithm can be nicely approximated by star-shaped sets [29, 38], see also Figure 1 for a visual comparison of binarized FIB-SEM image data (Figure 1b) and its representation as a union of star-shaped sets given by spherical harmonics (Figure 1d).

More precisely, the star shape allows for an identification of each sub-particle by a center $x_c \in \mathbb{R}^3$ and a function $\psi : [0,\pi] \times [0,2\pi) \to (0,\infty)$ on the unit sphere (given in polar coordinates). Then, for a star-shaped sub-particle $P_{x_c,\psi} \subset \mathbb{R}^3$ identified by x_c and ψ it holds that

$$P_{x_c,\psi} = x_c + \{y \in \mathbb{R}^3 : r(y) \leq \psi(\theta(y), \phi(y))\}, \tag{1}$$

where the vector $(r(y), \theta(y), \phi(y)) \in (0,\infty) \times [0,\pi] \times [0,2\pi)$ denotes the polar coordinates of $y \in \mathbb{R}^3$. Thus, the value $\psi(\theta,\phi)$ models the distance from x_c to the boundary of the set $P_{x_c,\psi} \subset \mathbb{R}^3$ in the direction given by (θ,ϕ).

Note that the radius function $\psi : [0,\pi] \times [0,2\pi) \to (0,\infty)$ considered in Equation (1) exhibits – under mild regularity conditions [28] – a representation as a series expansion with respect to spherical harmonics [27, 28]. In particular, if ψ is square integrable, then it admits the representation

$$\psi(\theta,\phi) = \lim_{L\to\infty} \sum_{\ell=0}^{L} \sum_{m=-\ell}^{\ell} c_\ell^m Y_\ell^m(\theta,\phi), \tag{2}$$

for all $(\theta,\phi) \in [0,\pi] \times [0,2\pi)$, where the complex number $c_\ell^m \in \mathbb{C}$ is called a spherical harmonics coefficient of ψ, and the function $Y_\ell^m : [0,\pi] \times [0,2\pi) \to \mathbb{C}$ denotes the spherical harmonics given by

$$Y_\ell^m(\theta,\phi) = \left(\frac{\sin\theta}{2}\right)^m \mathrm{e}^{\mathrm{i}m\phi} \sqrt{\frac{(2\ell+1)(\ell-m)}{4\pi(\ell+m)!}} \sum_{k=0}^{\ell-m} \frac{(m+l+k)!}{k!(m+k)!(\ell-m-k)!} \left(\frac{\cos\theta-1}{2}\right)^k, \tag{3}$$

for all integers m and ℓ fulfilling $0 \leq m \leq \ell$. For $-\ell \leq m < 0$, we define $Y_\ell^m(\theta,\phi) = (-1)^m\, Y_\ell^{-m}(\theta,\phi)$. Given ψ, the spherical harmonics coefficients $c_\ell^m \in \mathbb{C}$ can be obtained via

$$c_\ell^m = \int_0^{2\pi} \int_0^{\pi} \psi(\theta,\phi) \bar{Y}_\ell^m(\theta,\phi) \sin\theta \, \mathrm{d}\theta \mathrm{d}\phi, \tag{4}$$

where $\bar{Y}$ denotes the complex conjugate of $Y \in \mathbb{C}$.

To practically determine the star-shaped representation of sub-particles extracted from 3D image data, we estimate the values of c_ℓ^m for all $|m| \leq \ell \leq L$ and truncate the series in Equation (2) at $L = 10$. For this purpose, we proceed as in [29], where a detailed description of estimating the spherical harmonics coefficients from 3D image data is given.

A quantitative comparison of volume fractions and specific surface areas, which have been obtained for the solid phase of aggregate particles using binarized 3D FIB-SEM image data and the corresponding spherical harmonics representation, respectively, is given in Table A1 for the six samples described in Section 2, see also Figure A1 of Appendix A for a quantitative comparison of two-point coverage probability functions. Considering these geometrical descriptors, binarized 3D image data and the corresponding spherical harmonics representation nicely coincide.

3.2. Stochastic 3D model for the solid phase

We develop a parametric stochastic model for the 3D morphology of the nanostructured NMC particles, which is based on excursion sets of random fields, where we use tools from stochastic geometry [6] and mathematical morphology [7]. In particular, we consider excursion sets of so-called χ^2-fields with two degrees of freedom to model the solid phase of the nanostructured active material particles as described in Section 2. Note that we use χ^2-fields instead of the commonly considered Gaussian random fields [20–22], since it turned out that χ^2-fields are more appropriate to fit constrictivity, i.e. bottleneck effects, of the solid phase of the nanostructured NMC particles, see the results of model evaluation presented in Section 3.3 below.

To explain the notion of a χ^2-field with two degrees of freedom, we consider two independent copies X_1 and X_2 of a motion-invariant, *i.e.* stationary and isotropic, Gaussian random field $X = \{X(t), t \in \mathbb{R}^3\}$, whose expectation function $\mathbb{E}X : \mathbb{R}^3 \to \mathbb{R}$ and variance function $\mathsf{Var}X : \mathbb{R}^3 \to [0,\infty)$ fulfill $\mathbb{E}X(t) = 0$ and $\mathsf{Var}X(t) = 1$ for each $t \in \mathbb{R}^3$. Another important characteristic of X is its covariance function $\rho_X : [0,\infty) \to [-1,1]$, which is given by $\rho_X(h) = \mathsf{Cov}(X(s), X(t))$ for each $h > 0$, where $s, t \in \mathbb{R}^3$ with $|s - t| = h$. Due to the assumed motion invariance of X, the value of $\rho_X(h)$ does not depend on the particular

choice of s and t. Moreover, note that motion-invariant Gaussian random fields are uniquely determined by the expectation $\mathbb{E}X(o)$, where $o \in \mathbb{R}^3$ denotes the origin, and the correlation function ρ_X. For further information regarding Gaussian random fields, the reader is referred to [6, 39].

Using the Gaussian random fields X_1 and X_2, we can define the random field $Y = \{Y(t), t \in \mathbb{R}^3\}$ by putting $Y(t) = X_1^2(t) + X_2^2(t)$ for each $t \in \mathbb{R}^3$, where Y is called a χ^2-field with two degrees of freedom. Note that, like the Gaussian random field X, the χ^2-field Y is uniquely determined by the expectation $\mathbb{E}X(o)$ and the correlation function ρ_X of X.

The solid phase of nanostructured active material particles is then modeled by the (random) excursion set $\Xi = \{t \in \mathbb{R}^3 : Y(t) \geq \lambda\}$ for some $\lambda > 0$. In order to fit λ (and further model parameters) to the 3D image data described in Section 2, we use analytical relationships between these parameters and geometrical descriptors which can easily be extracted from 3D image data. For this purpose, we consider the volume fraction $p = \mathbb{E}\nu(\Xi \cap [0,1]^3)$ of the (motion-invariant) random set Ξ, where $\nu(\Xi \cap [0,1]^3)$ denotes the volume of the set $\Xi \cap [0,1]^3 \subset \mathbb{R}^3$, as well as its two-point coverage probability function $C : [0,\infty) \to [0,1]$ defined by $C(h) = \mathbb{P}(s \in \Xi, t \in \Xi)$ for each $h = |s - t| \geq 0$. Analogously to the invariance property of the covariance function ρ_X of X mentioned above, the value of $C(h) = C(|t - s|)$ does not depend on the particular choice of t and s. Moreover, the following formulas are true. First, we make use of the fact that

$$p = \mathbb{P}(o \in \Xi) = \mathbb{P}(Y(o) \geq \lambda), \tag{5}$$

see Equation (6.34) in [6], and we exploit the following relationship.

Proposition 1. *The two-point coverage probability function $C : [0,\infty) \to [0,1]$ of the random excursion set Ξ fulfills*

$$C(h) = 2p - 1 + (1 - \rho_X^2(h)) \sum_{j=0}^{\infty} \frac{\rho_X^{2j}(h)}{(j!)^2} \left(\int_0^{\frac{\lambda}{2(1-\rho_X^2(h))}} t^j \exp(-t) \mathrm{d}t \right)^2, \tag{6}$$

for each $h > 0$.

To the best of our knowledge, so far relationships of the form given in Equation (6) are available in the literature only for the cases, when Y is either Gaussian or a χ^2-field with one degree of freedom, see Equations (6.158) and (6.160) in [6], respectively.

A proof of Proposition 1 is given in Appendix B. Note that for each $h > 0$, the value of $C(h)$ is monotonically increasing for increasing values of $\rho_X(h) \in [0,1]$. This follows directly

from a Slepian-type result for random variables, which can be represented as compositions of random variables with elliptically contoured distributions, see Theorem 4.3 in [40]. Due to this result, it is possible for each $h > 0$, to numerically solve Equation (6) for $\rho_X(h)$ by the method of bisection. This means that Proposition 1 allows for determining the covariance function ρ_X based on the knowledge of the two-point coverage probability function C, which can be directly estimated from image data as described in Chapter 6 of [41].

3.3. Calibration and validation of the stochastic 3D model

We now assume that the covariance function of X has the form $\rho_X(h) = \exp(-\alpha^2 h)$ for each $h > 0$, where $\alpha > 0$ is some parameter. Thus, to calibrate the stochastic 3D model for the FIB-SEM image data described in Section 2, we have to compute estimates of the model parameters λ and α. First, in order to estimate λ, we use Equation (5). This leads to the estimator

$$\widehat{\lambda} = \chi^2_{2,1-\widehat{p}}, \tag{7}$$

where $\chi^2_{2,1-\widehat{p}}$ denotes the $1-\widehat{p}$ quantile of the χ^2-distribution with two degrees of freedom. Here $\widehat{p}$ denotes an estimator for the volume fraction $p = \mathbb{E}|\Xi \cap [0,1]^3|$ of Ξ, which is obtained by the so-called point-count method, see Section 6.4.2 in [6]. Then, to estimate α, we use the analytical relationship between C and ρ_X stated in Proposition 1, where Equation (6) is numerically solved for $\rho_X(h)$ after replacing the two-point coverage probability $C(h)$ by an appropriately chosen estimate $\widehat{C}(h)$. The values obtained in this way for the estimators $\widehat{\lambda}$ and $\widehat{\alpha}$ are provided in Table 1, together with the volume fractions estimated from binarized 3D FIB-SEM image data for the six samples described in Section 2.

Table 1: Estimated values for p, λ and α, computed from binarized 3D FIB-SEM image data.

Parameter	F850	F900	M850	M900	C850	C900
$\widehat{p}$	0.46	0.68	0.52	0.60	0.62	0.70
$\widehat{\lambda}$	1.55	0.77	1.31	1.02	0.96	0.71
$\widehat{\alpha}/\mu\text{m}^{-1}$	7.28	4.63	6.01	4.27	5.47	3.49

Visual comparison of binarized 3D FIB-SEM image data with realizations drawn from the stochastic 3D models, which have been fitted to the 3D FIB-SEM data, shows a quite good accordance, see Figure 2. Furthermore, the fitted 3D models are quantitatively validated by comparing geometrical descriptors of model realizations with those computed from the 3D FIB-SEM data. For this purpose, ten model realizations with a size of 4 µm×4 µm×4 µm are drawn from each of the six model specifications fitted to the particle samples as described

above. Then, for each model specification, various geometrical descriptors are computed for each of the then model realizations and, finally, averaging over these ten realizations is performed.

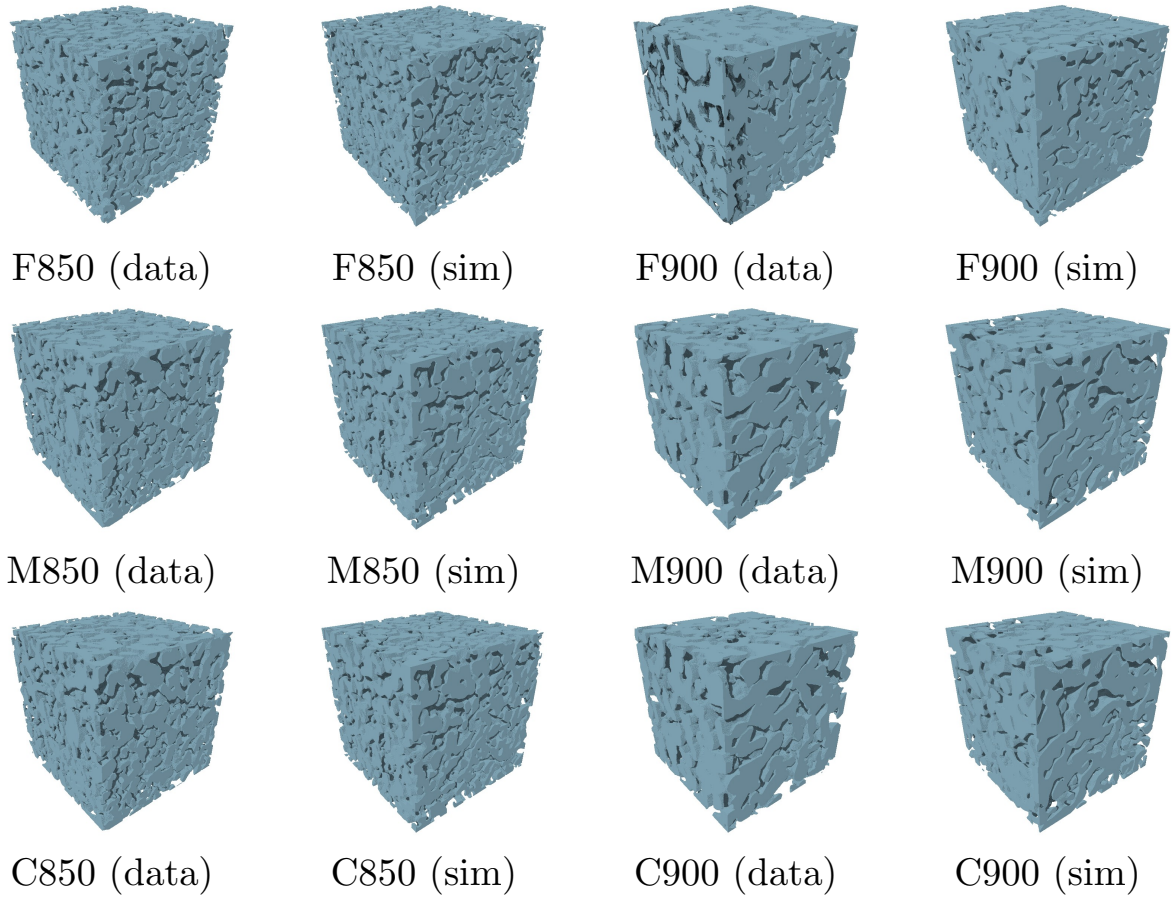

Figure 2: Visual comparison between tomographic image data and simulated model realizations.

To quantitatively validate the fitted 3D models, we investigate the following geometrical descriptors of the nanostructured NMC particles. In particular, we consider the volume fraction p of the solid phase, as well as the specific surface area S, which is estimated from discrete 3D image data as described in Section 5.2 of [41]. Moreover, we consider the mean geodesic tortuosity τ_{geod} and constrictivity β of both, the solid phase and the pore phase. The notion of mean geodesic tortuosity of a materials phase (solid or pores) is given as the quotient of the expected length of shortest paths through the material, which are fully contained in the phase under consideration, divided by the thickness of the material. Note that mean geodesic tortuosity is a purely geometrical descriptor, while the so-called effective tortuosity characterizing transport phenomena in a given structure is considered in Sections 4.2 and 4.3.

Beyond that there are many different notions of tortuosity used in the literature. For an overview, we refer to [42]. The constrictivity β is a descriptor for the strength of bottlenecks effects, given as squared ratio of the width of the typical bottleneck obtained from simulated mercury intrusion porosimetry over the median of the continuous phase size distribution, see e.g. [43] for details. A formal definition of mean geodesic tortuosity and constrictivity in the framework of stationary random sets can be found in [22].

The values given in Table 2 show that the volume fraction of the solid phase as well as mean geodesic tortuosities of pores and solid are nearly identical when comparing the results obtained for model realizations and tomographic image data, respectively. For the volume fraction p of the solid phase, this is not surprising since the parameter λ defining the level of the excursion set was fitted in order to match the volume fraction, see Equation (7). Mean geodesic tortuosity, however, as well as specific surface area and constrictivity are not used for model fitting. For the latter two descriptors, slight discrepancies between the values obtained for model realizations and tomographic image data can be observed, see Table 2. The specific surface area S is slightly overestimated by the models (except of the case with coarse particles calcined at 900°C), while the qualitative trend observed in tomographic image data is reproduced, i.e., the values of S become smaller with coarser particles and the increase of calcination temperature from 850°C to 900°C. With respect to constrictivity, the goodness-of-fit depends on the sample under consideration. While a nearly perfect fit is obtained in the cases of F850 (solid and pores), F900 (solid), M850 (pores) and M900 (solid), slightly larger deviations are observed for the other samples up to a relative error of 17 % for M900 (pores). However, it will be shown in Section 5.1 that despite of these deviations, the numerically simulated effective conductivities of the solid phase and the effective diffusivities of the pore space are in good agreement when comparing the values obtained for simulated model realizations with those for the corresponding 3D image data. We refer to Appendix C, where we show that both, the SEM images as well as the sample sizes of the virtual microstructures are representative.

Table 2: Values of geometrical descriptors computed from tomographic image data and simulated model realizations, respectively.

Sample	p	$S/\mu\text{m}^{-1}$	τ_{geod} (solid)	τ_{geod} (pores)	β (solid)	β (pores)
F850 (data)	0.46	8.44	1.10	1.05	0.51	0.68
F850 (sim)	0.46	9.34	1.11	1.05	0.53	0.68
F900 (data)	0.68	5.75	1.05	1.13	0.61	0.55
F900 (sim)	0.68	6.23	1.05	1.11	0.61	0.63
M850 (data)	0.52	7.80	1.10	1.07	0.47	0.67
M850 (sim)	0.52	8.04	1.09	1.07	0.54	0.68
M900 (data)	0.60	5.27	1.07	1.09	0.55	0.58
M900 (sim)	0.60	5.82	1.07	1.09	0.57	0.66
C850 (data)	0.62	7.14	1.06	1.09	0.55	0.58
C850 (sim)	0.62	7.46	1.06	1.09	0.60	0.66
C900 (data)	0.70	4.72	1.05	1.12	0.53	0.52
C900 (sim)	0.70	4.66	1.05	1.12	0.62	0.61

Furthermore, the goodness-of-fit of the calibrated stochastic 3D models is analyzed with respect to the two-point coverage probability function $C : [0, \infty) \to [0, 1]$. More precisely, the centered two-point coverage probability function $C_0 : [0, \infty) \to [-1, 1]$ given by $C_0(h) = C(h) - p^2$ is considered. Note that the closer, the centered two-point coverage probability $C_0(h)$ is to zero, the less pronounced is the spatial dependence of the events that $s \in \Xi$ and $t \in \Xi$ for points $s, t \in \mathbb{R}^3$ of distance $h = |t - s| > 0$ from each other. In Figure 3, one the functions C_0 computed from tomographic image data are compared with the average curve from 10 model realizations. There are slight deviations for some samples. Nevertheless, keeping in mind that one and the same model type (with only two parameters) is fitted to all six differently manufactured samples, we consider the results in Figure 3 as a good fit.

This justifies our parametric model choice for the covariance function ρ_X, i.e., assuming that $\rho(h) = \exp(-\alpha^2 h)$ for $h > 0$. Thus, it can be ascertained that the 3D morphology of the nanostructured active material considered in this paper can be nicely modeled by a relatively simple stochastic 3D model with only two model parameters, namely the level λ of the random excursion set Ξ and the parameter α appearing in the covariance function of the underlying Gaussian random field X.

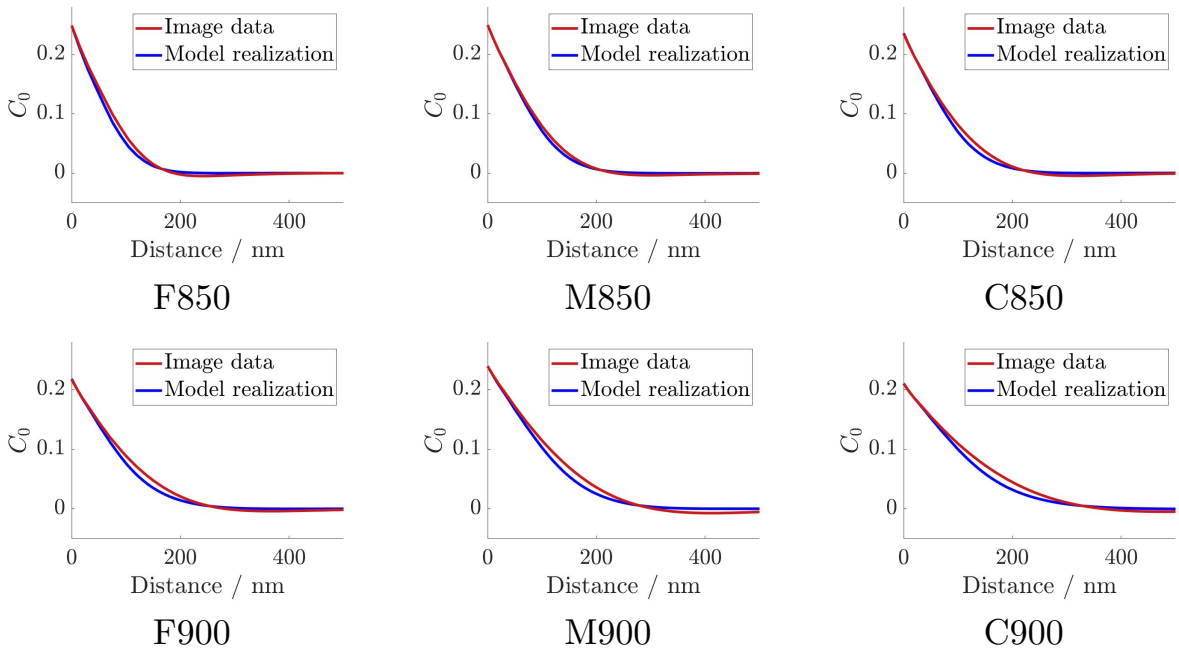

Figure 3: Centered two-point coverage probability functions for FIB-SEM image data and the average curve over 10 model realizations. The comparison is shown for all samples.

4. Numerical modeling of effective transport properties

For hierarchically structured battery electrodes, where the 3D morphology on different length scales influences the performance of the cell, multi-scale approaches are exploited for numerical modeling. For this purpose, effective transport properties of the micro- and nanoscale are used as aggregated information for numerical modeling on the macroscopic scale. For the materials considered in the present paper, the effective diffusion coefficients of ionic and electric transport within nanostructured NMC particles are crucial quantities on the nanoscale. In the present paper, we focus on limitations of the electric transport in the solid phase arising due to the nanopores and do not consider the influence of the polycristalline grain architecture, experimentally investigated in [44].

4.1. Intrinsic versus effective transport coefficients

There are different mathematical methods to determine effective transport coefficients [45–47]. A common approach is to scale the intrinsic transport coefficients. The scaling factors obtained in this way account for transport processes within nanostructured active material particles being limited by their morphology on the nanoscale. For example, the diffusion of ions in the pore space is hindered, in comparison to a straight path, by the windedness

of transportation paths of ions through the nanostructured active material particles. This effect is quantified by the notion of mean geodesic tortuosity mentioned in Section 3.3. In the present paper, we consider electric conduction in the solid phase and ionic diffusion in the pores of nanostructured active material particles, where the mathematical concepts of these two transport phenomena coincide.

Note that the direct comparison of the flux of a transport problem on two different length scales is a common approach to determine the scaling factor corresponding to the effective transport coefficient in the material phase under consideration, *i.e.*, the pore space for ionic diffusion in the electrolyte and the solid phase for the electric conduction. For this, one needs to compute the flux on a domain $\Omega_{\text{ref}} \subset \mathbb{R}^3$, which is considered as the material phase (pores or solid) where transport occurs. The domain Ω_{ref} is assumed to be contained in a rectangular cuboid $\Omega_{\text{hom}} \subset \mathbb{R}^3$, see Figure 4. The cuboid Ω_{hom} is then used to solve the so-called homogenized problem, where the top, bottom and side surfaces of Ω_{hom} are denoted by Γ_u, Γ_d and Γ_0, respectively, see Figure 4.

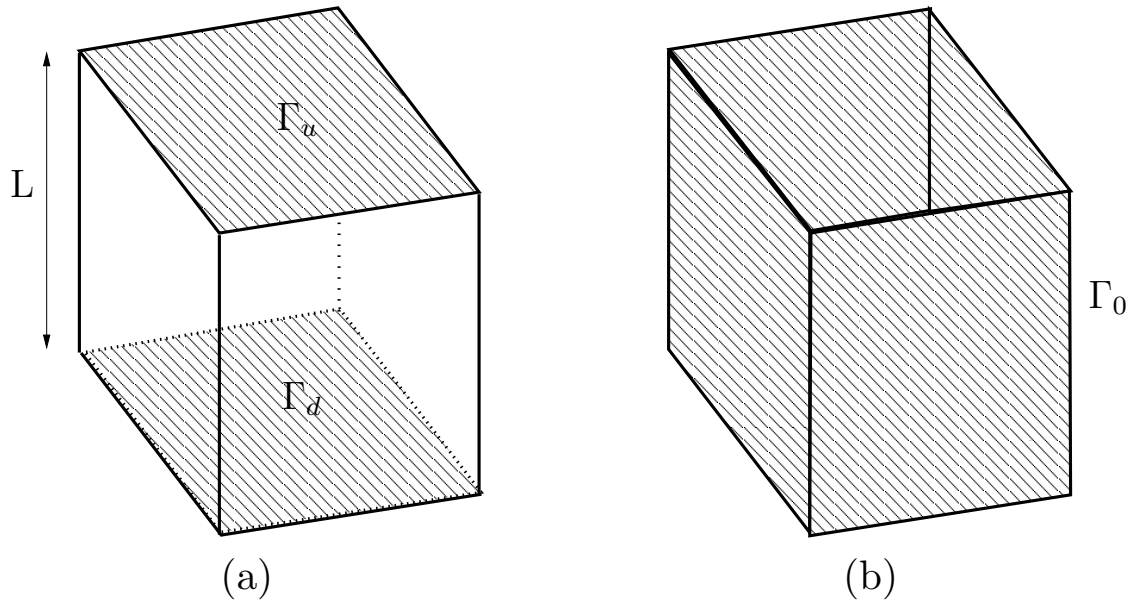

Figure 4: Schematic representation of outer surfaces of the homogeneous volume Ω_{hom}, where different boundary conditions are applied: Dirichlet boundary conditions to the top and bottom surfaces (a), and a Neumann condition of zero flux to the side surfaces (b).

The domain Ω_{ref} is taken as reference volume of the nanostructure, where the diffusion tensor is approximated by a diagonal tensor such that each component is determined by solving a diffusion problem with respect to a main transport direction. More precisely, this

diffusion problem for the nanostructure is treated by solving

$$\nabla \cdot (D \nabla u) = 0 \qquad \text{in } \Omega_{\text{ref}}, \tag{8}$$

for $u : \Omega_{\text{ref}} \to \mathbb{R}$, where $D > 0$ is the intrinsic transport coefficient (of either electric conduction or ionic diffusion), and with Dirichlet conditions in the main transport direction and no-flux conditions on the rest of surfaces of Ω_{ref}. For example, considering the main transport along the $(0, 0, -1)$-direction from top to bottom, see Figure 4, Dirichlet boundary conditions apply to the top surface $\Gamma_u \cap \Omega_{\text{ref}}$ and the bottom surface $\Gamma_d \cap \Omega_{\text{ref}}$ of Ω_{ref}, *i.e.*, $u(x) = 1$ for $x \in \Gamma_u \cap \Omega_{\text{ref}}$ and $u(x) = 0$ for $x \in \Gamma_d \cap \Omega_{\text{ref}}$, and a Neumann condition of zero flux is applied to the rest of the outer surface $\Gamma_0 \cap \Omega_{\text{ref}}$ (and to the inner interface between solid and pore phase, not shown in Figure 4). Note that the solution $u : \Omega_{\text{ref}} \to \mathbb{R}$ of Equation (8) describes the spatially resolved ion concentration or electric potential in the material phase under consideration, in dependence on whether ionic diffusion or electric conduction is considered.

To determine the effective transport coefficient $D_{\text{eff}} > 0$, the flux of the transport problem within the nanostructure is compared to the flux of the homogenized problem, where the difference between these two problems is just induced by the different domains. Recall that in Equation (8) the nanostructure domain Ω_{ref} is considered, while for solving the homogenized problem

$$\nabla \cdot (D_{\text{eff}} \nabla w) = 0 \qquad \text{in } \Omega_{\text{hom}}, \tag{9}$$

for $w : \Omega_{\text{hom}} \to \mathbb{R}$, the nanostructure is not taken into account. However, similarly to the diffusion problem considered in Equation (8), the boundary conditions of Equation (9) are Dirichlet conditions in the main transport direction and the no-flux condition on the side surfaces of Ω_{hom}. The solution of the homogenized problem stated in Equation (9) can be determined analytically. If one is interested in transport along the $(0, 0, -1)$-direction, the solution is given by $w : \Omega_{\text{hom}} \to \mathbb{R}$ with $w(x) = x_3/L$, where $x = (x_1, x_2, x_3) \in \mathbb{R}^3$ is the position vector and $L > 0$ denotes the edge length of the cuboid Ω_{hom} in $(0, 0, -1)$-direction, see Figure 4.

The fluxes $J_{\text{nano}}, J_{\text{hom}} \geq 0$ of the two problems described above are then given by

$$J_{\text{nano}} = D \int_A \frac{\partial u(x)}{\partial n} \, \mathcal{H}_2(\mathrm{d}x) \quad \text{and} \quad J_{\text{hom}} = D_{\text{eff}} \int_A \frac{\partial w(x)}{\partial n} \, \mathcal{H}_2(\mathrm{d}x) = D_{\text{eff}} \frac{\mathcal{H}_2(A)}{L}, \tag{10}$$

where $\mathcal{H}_2$ denotes the two-dimensional Hausdorff measure, $A \subset \Omega_{\text{ref}}$ is an arbitrary planar section of the domain Ω_{ref} orthogonal to the $(0,0,-1)$-direction with area $\mathcal{H}_2(A) > 0$, and $n = (0,0,-1)$ denotes the unit normal vector to this planar section. Note that the specific choice of the planar cross section $A \subset \Omega_{\text{ref}}$ is arbitrary due to the divergence theorem, since the solutions of Equations (8) and (9) are divergence-free and no-flux conditions are applied on the inner and side surfaces of Ω_{ref} and Ω_{hom}, respectively. By identifying the fluxes J_{nano} and J_{hom}, *i.e.*, putting $J_{\text{hom}} = J_{\text{nano}}$, we get that

$$D_{\text{eff}} = J_{\text{nano}} \frac{L}{\mathcal{H}_2(A)}. \tag{11}$$

4.2. Numerical computation of the effective transport coefficient using level sets

The effective transport coefficient D_{eff} as described in Section 4.1 is computed by numerically solving Equation (8), where we use the finite element method on a regular grid. For this purpose, the domain Ω_{eff} of the material phase under consideration is represented by a union of sub-particles, where the outer shell of each sub-particle is approximated by a series expansion with respect to spherical harmonics, see Section 3.1. Then, for each sub-particle $P_{x_c,\psi} \subset \mathbb{R}^3$ with center at $x_c \in \mathbb{R}^3$ and radius function ψ, we consider the (centered) distance function $\varphi_{x_c} : \mathbb{R}^3 \to \mathbb{R}$ given by $\varphi_{x_c}(x) = |x - x_c| - \psi_{\text{cart}}(x)$ for each $x \in \mathbb{R}^3$, where $\psi_{\text{cart}}(x) = \psi(\theta, \phi)$ is the value of the radius function ψ at $x \in \mathbb{R}^3$ and the angles $(\theta, \phi) \in [0, 2\pi) \times [0, \pi]$ denote the spherical coordinates of x (with respect to the reference point x_c). Note that $x \in \mathbb{R}^3$ belongs to the inner part or the boundary of $P_{x_c,\psi}$ if $\varphi_{x_c}(x) < 0$ or $\varphi_{x_c}(x) = 0$, respectively. Therefore, the sub-particle $P_{x_c,\psi}$ can be represented by a level set, *i.e.*,

$$P_{x_c,\varphi} = \{x \in \mathbb{R}^3 : \varphi_{x_c}(x) \leq 0\}. \tag{12}$$

A particular advantage of the level-set approach described above, based on spherical harmonics expansions of the radius functions of the sub-particles constituting the domain Ω_{ref}, is the possibility to arbitrarily adjust the grid size (as long as computationally feasible) when numerically solving Equation (8). Moreover, this approach can be used for the generation of locally adapted mesh grids as an input for the finite element method [48, 49].

To construct a computational grid for solving Equation (8) on the nano-scale, a subdivision of the domain Ω_{hom} into a regular uniform hexahedral grid is performed. In our case, this grid coincides with the voxel grid given by the image data. Based on the values of the distance functions φ_{x_c} evaluated at the nodes of this grid, an approximation of the domain Ω_{ref} representing the nanostructure is defined. However, there can be cells of the grid where

the distance function φ_{x_c} vanishes on a set of points within the cell, for some sub-particle $P_{x_c,\psi}$. These cells are assigned to a given material phase (pores or solid) if the major part of their volume belongs to that material phase.

Now, inserting the numerical solution $u : \Omega_{\text{ref}} \to \mathbb{R}$ of Equation (8) into Equation (10), the flux J_{hom} and, using Equation (11), the effective transport coefficient D_{eff} can be computed. However, instead of D_{eff}, the notion of effective tortuosity (denoted by τ_{eff} in the following) is frequently used in multiscale models, like in the-well known pseudo-two-dimensional (P2D) Doyle-Fuller-Newmann model [50], where τ_{eff} can easily be expressed by D_{eff} via the relationship

$$\tau_{\text{eff}} = \frac{\varepsilon}{D_{\text{eff}}} D. \tag{13}$$

Here ε denotes the volume fraction of the material phase under consideration, *i.e.*, $\varepsilon = p$ and $\varepsilon = 1 - p$ when transport in the solid phase and the pore space, respectively, is considered. Thus, using Equations (10), (11) and (13), the effective tortuosity τ_{eff} can be computed, where

$$\tau_{\text{eff}} = \varepsilon D \frac{\mathcal{H}_2(A)}{L\, J_{\text{nano}}} \qquad \text{and, equivalently,} \qquad \tau_{\text{eff}} = \varepsilon \frac{\mathcal{H}_2(A)}{L \int_A \frac{\partial u(x)}{\partial n}\, \mathcal{H}_2(\mathrm{d}x)}.$$

Note that the solution $u : \Omega_{\text{ref}} \to \mathbb{R}$ of Equation (8) does not depend on the intrinsic transport coefficient D, since D is assumed to be constant, *i.e.*, not location-dependent. Thus, from the latter representation formula for τ_{eff}, it can be concluded that τ_{eff} also does not depend on D.

4.3. M-factor for predicting the microstructure influence on effective transport

Besides the effective transport coefficient D_{eff} and the effective tortuosity τ_{eff}, there still is a third quantity, which can be used to characterize transport processes in porous media. This is the so-called M-factor, see e.g. [42], which is the ratio of effective over intrinsic conductivity, when the solid phase is considered, and the ratio of effective over the intrinsic diffusivity in the case of the pore space. Formally, the M-factor $0 \leq M \leq 1$ is given by

$$M = \frac{D_{\text{eff}}}{D} \qquad \text{or, equivalently,} \qquad M = \frac{\varepsilon}{\tau_{\text{eff}}}. \tag{14}$$

In [33], an empirically derived relationship between the M-factor and three morphological descriptors (volume fraction ε, mean geodesic tortuosity τ_{geod} and constrictivity β) of the

transporting phase has been investigated, where the predictor

$$\widehat{M} = \frac{\varepsilon^{1.15}\,\beta^{0.35}}{\tau_{\mathrm{geod}}^{4.39}} \tag{15}$$

of the M-factor defined in Equation (14) is considered. A detailed discussion of the predictive power of the quantity $\widehat{M}$ given in Equation (15) is provided in [30], see also [31, 32].

Although the (simulated) 3D morphologies, on the basis of which Equation (15) has been derived in [33], differ from those of nanostructured active materials, it turns out that the predictor $\widehat{M}$ given in Equation (15) is also suitable for the 3D morpohologies considered in the present paper. Moreover, the M-factor can be be used to evaluate the stochastic 3D model introduced in Section 3.2, by comparing the effective transport coefficients computed for tomographic image data and simulated 3D nanostructures of NMC particles, see Section 5.

5. Process-structure-property relationships

This section is devoted to process-structure-property relationships of nanoporous NMC particles. First, we validate the stochastic 3D model introduced in Section 3.2 in terms of effective transport properties, see Section 5.1. Then, in Section 5.2, we show that previously derived structure-property relationships [30, 33] are valid to quantify the influence of the 3D morphology of the nanostructured active material on its effective conductivity and effective diffusivity. Finally, in Section 5.3, we discuss the influence of manufacturing parameters (particle size and calcination temperature) on effective transport properties.

5.1. Validation of the stochastic 3D model in terms of effective transport properties

Recall that in order to compute the M-factor for tomographic image data and virtual (simulated) nanoporous NMC particles, we represent their solid phase as a union of sub-particles, the outer shell of which is given by a series expansion with respect to spherical harmonics as described in Section 3.1. Doing so, we obtain an analytical representation of the nanostructured active material. Based on this representation, for each of the six samples F850, M850, C850, F900, M900, and C900, the M-factors of the solid phase and the pore space are numerically computed for tomographic image data and for five model realizations drawn from the correspondingly calibrated stochastic 3D model described in Section 3.2.[1]

[1]Here we use five of the ten realizations, which have been drawn from the stochastic 3D model, see Section 3.3. Recall that these realizations have a size of 4 µm × 4 µm × 4 µm.

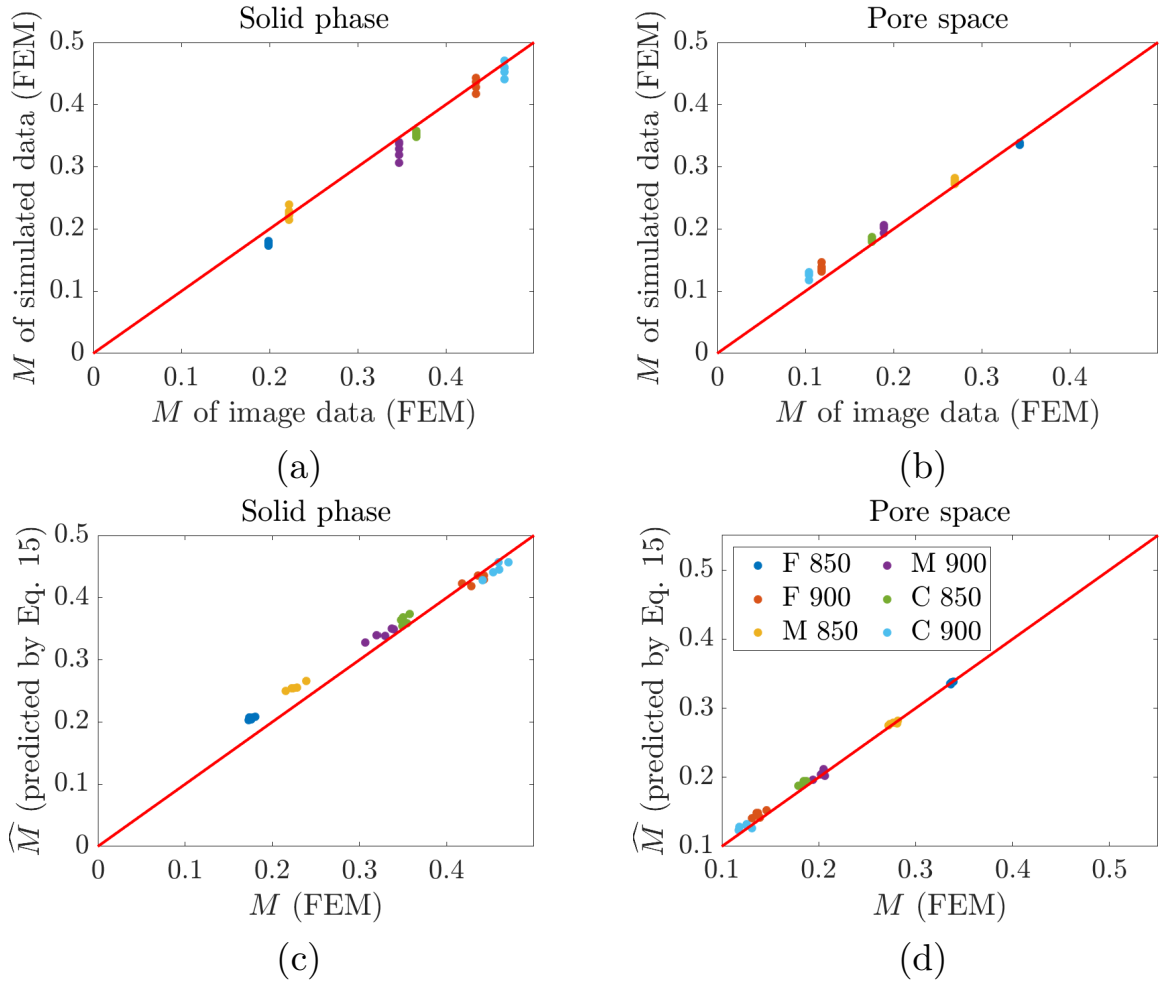

Figure 5: Comparison of model realizations and tomographic image data in terms of numerically computed M-factors for solid phase (a) and pore space (b). The data points with one and the same color correspond to the different model realizations (five per sample) drawn from the correspondingly calibrated stochastic 3D model. Comparison of geometrically predicted and numerically computed M-factors for solid phase (c) and pore space (d) of the 30 model realizations.

For this purpose, FEM has been used as described in Section 4.2, where, in total, we consider 36 datasets for six different scenarios, defined by particle size and calcination temperature.

In Figures 5, the results are compared which we obtained for the M-factors computed on tomographic image data and on virtual nanostructures, respectively, for both, solid phase (Figure 5a) and pore space (Figure 5b). It can be observed that the M-factors of the model realizations reproduce those of the tomographic image data quite well. Thus, this comparison further validates the stochastic 3D model and, in particular, complements the validation performed in Section 3.2 by means of morphological descriptors. The additional model validation in terms of effective transport properties also shows that the deviations observed for constrictivity (see Table 2) are relatively small such that the fit of the M-factor is still good. On the other hand, note that there is some variability within the M-factors computed for the five realizations of each sample. However, this variability is small enough such that there is no major overlap between the M-factors of different samples. This shows that the representative volume element has been chosen large enough in order to distinguish between the different samples in terms of effective transport properties.

5.2. Predicting the M-factor from morphological descriptors

A comparison of geometrically predicted and numerically computed M-factors for solid phase and pore space of the 30 model realizations is given in Figures 5c and 5d, respectively, where the geometrical predictor $\widehat{M}$ is determined by means of Equation (15). It turns out that the quality of the predictor $\widehat{M}$ is quite good, which shows that Equation (15) is suitable for a larger class of 3D morphologies than the one originally used in [33], where the prediction formula given in Equation (15) has been derived. As a further result in this direction, it has been shown in [51] that Equation (15) leads to good predictions for the effective diffusivity in porous silica.

5.3. The influence of manufacturing parameters on effective transport properties

Figure 5 also shows the influence of parameters of the manufacturing process on effective transport properties. For a fixed particle size, an increase of the calcination temperature leads to an increase of the M-factor computed for the solid phase. The difference between the M-factors computed for calcination temperatures of 850°C and 900°C, respectively, is the greater the finer the particles are. An analogous behavior is observed for the M-factors of the pore space, which show a qualitatively opposite trend compared to the M-factors of the solid phase. A more detailed discussion of the influence of manufacturing parameters, which goes beyond transport properties within nanostructured active material particles, can

be found in [5]. In particular, it is shown there that the M-factor of the solid phase has a stronger influence on the electrode performance than the M-factor of the pore space. Among the cathodes considered in the present work, those with coarse active material particles also have a larger specific capacity than those cathodes with fine active material particles (in addition to the larger M-factors of the solid phase). Moreover, their specific capacity is larger than that of a reference cathode fabricated without nanostructuring, see Figure 3 in [5]. It is important to note that for performance indicators such as specific capacity, the spatial arrangement of all active material particles and the binder-additive phase within the electrode also plays a crucial role. Detailed investigations with respect to the influence of the binder-additive phase in lithium-ion batteries can be found, e.g., in [52, 53].

6. Conclusion

In the present paper, we have developed a data-driven modeling approach to efficiently investigate process-structure-property relationships of nanostructured active material particles for cathodes in lithium-ion batteries. For this purpose, a stochastic 3D nanostructure model with only two parameter has been developed which allows for the generation of digital twins of differently manufactured active material particles, the morphology of which is resolved by FIB-SEM tomography. Model validation is performed by comparing model realizations with image data in terms of morphological descriptors not used for model fitting. Even if slight deviations with respect to constricitivity are observed for some samples, the overall fit is good.

Moreover, when using finite element modeling to compute effective transport properties of the considered materials, we observe a nearly perfect match between model realizations and image data regarding effective conductivity of the solid phase and effective diffusivity in the pore space. In addition to the performed model validation, we show that structure-property relationships, which have been established for other types of morphologies in previous publications [30, 33], are also valid for the nanostructured active material particles investigated in the present paper. Considering the absolute values of effective conductivity of the solid phase and effective diffusivity in the pore space, we observe that the impact of increasing the calcination temperature from 850°C to 900°C becomes less pronounced with an increasing particle size. In future work, a variation of the parameters of the stochastic 3D nanostructure model can be used to generate a large data basis of virtual nanostructured active materials which allows, *e.g.*, to efficiently study the impact of porosity on effective transport properties by means of numerical simulation.

For the samples considered in this study, it has been shown in [5] that coarse particles lead to the best specific capacity. The modeling and simulation approach developed in the present paper is a further step towards an in-deepth investigation of hierarchically structured cathode materials using detailed morphological information on the nanometer scale. In particular, the effective transport properties of nanostructured active material particles determined in the present paper can be used as an input for models on the electrode scale with homogenized properties of active material particles [54, 55], which, in turn, provides input for models on the macro-scale as the P2D-model. With such an up-scaling, modeling and simulation can then also be used to study relationships between parameters of the manufacturing process and performance indicators such as the specific capacity.

Note that the original P2D-model [56] uses an effective transport coefficient at the electrode level and an intrinsic transport coefficient for the active material particles, since the latter are not considered porous. As a possible application of our approach, we consider the extension of the P2D-model published in [57], where the active material particles themselves are porous. This model has two effective transport coefficients, one for the electrode scale and one for the nanostructured active material particles. The effective conductivity of the electrodes, which can be measured while considering the particles arrangement and their nanostructure, cannot be used to separate the effect of the internal porosity of the active material particles. The latter affects the behavior of the nanostructured active material particles and is visible in the measurements shown in [5]. The separate quantification of the effective conductivity at the electrode and particle scales shows that the electronic conduction inside the nanostructured active material particles becomes the limiting transport process and explains the influence of the manufacturing parameters, namely calcination temperature and particle size. The additional efforts to determine the properties of the nanostructured active material particles as made in the present paper, together with the simulations of their behavior, can increase the identifiability and validity of P2D-models.

Acknowledgements

This work has been supported by the German Federal Ministry for Economic Affairs and Climate Action (BMWK) and granted through Project Management Jülich (03ETE039A, 03ETE039G, 03ETE039H, 03ETE039J). Moreover, this work was partially funded by the German Research Foundation (DFG) within the framework of SPP 2248 “Polymer-based batteries” (CA 633/4-1 , MA 5039/7-1, SCHM 997/39-1). The work by MN was funded by DFG under Project ID 390874152 (POLiS Cluster of Excellence, EXC 2154). The present

paper contributes to the research performed at CELEST (Center for Electrochemical Energy Storage Ulm-Karlsruhe).

Appendix A: Validation of approximation by spherical harmonics expansions

We provide a quantitative validation of the spherical harmonics approximation of the solid phase, as described in Section 3.1. For this purpose, we compare the nanostructure descriptors volume fraction and specific surface area (Table A1) as well as the centered two-point coverage probability functions (Figure A1) of binarized image data with the corresponding discretization of the spherical harmonics representation. For the discretization, we use the same voxel size as in the underlying FIB-SEM data. For a definition of the respective nanostructure descriptors, see Sections 3.2 and 3.3.

	Volume fraction		Surface area per unit volume / μm^{-1}	
Sample	Image data	Spherical harmonics	Image data	Spherical harmonics
F850	0.4636	0.4768	8.445	8.365
F900	0.6821	0.6970	5.754	5.976
M850	0.5241	0.5378	7.810	7.868
M900	0.6038	0.6196	5.269	5.407
C850	0.6237	0.6371	7.149	7.230
C900	0.6988	0.7143	4.737	4.579

Table A1: Comparison of volume fractions and specific surface areas, computed from binarized 3D FIB-SEM image data and the corresponding spherical harmonics representation, respectively.

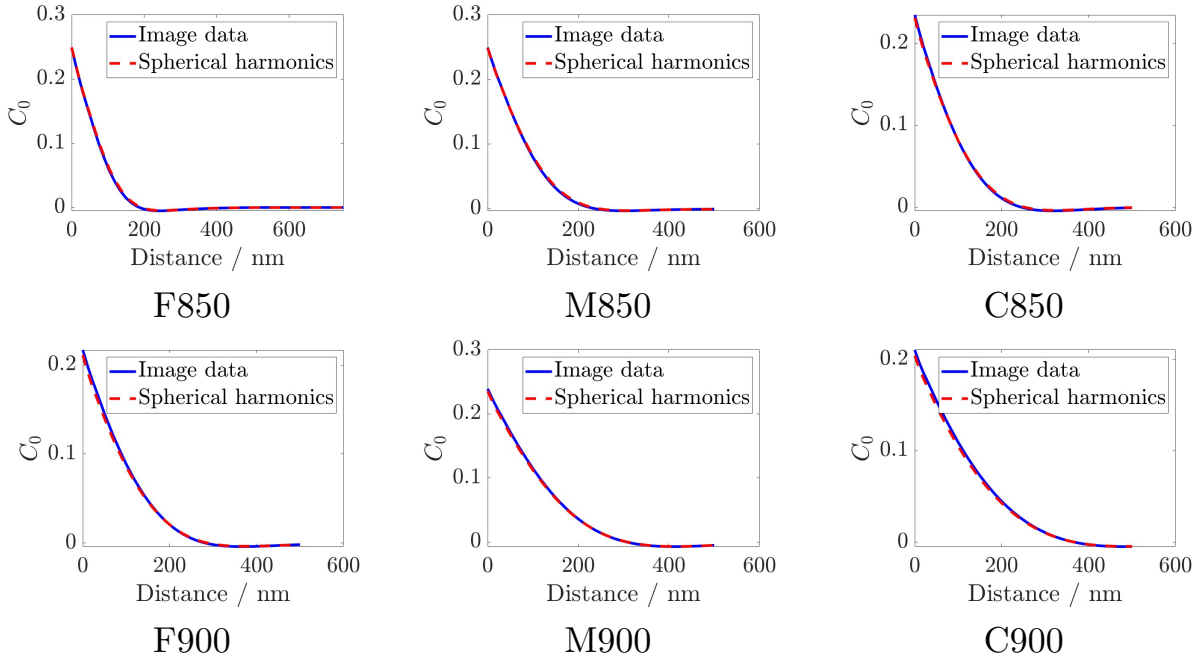

Figure A1: Comparison of centered two-point coverage probability functions computed from binarized 3D FIB-SEM image data (blue) and the corresponding spherical harmonics representation (red).

Appendix B: Proof of Proposition 1

For any $\lambda > 0$ and $t \in \mathbb{R}^3$ with $|t| = h$, we have

$$\begin{aligned} C(h) &= \mathbb{P}(o \in \Xi, t \in \Xi) \\ &= \mathbb{P}(Y(o) \geq \lambda, Y(t) \geq \lambda) \\ &= 1 - 2\mathbb{P}(Y(o) < \lambda, Y(t) \geq \lambda) - \mathbb{P}(Y(o) < \lambda, Y(t) < \lambda) \\ &= 1 - 2\mathbb{P}(Y(o) < \lambda, Y(t) \geq \lambda) - 2\mathbb{P}(Y(o) < \lambda, Y(t) < \lambda) \\ &\quad + 2\mathbb{P}(Y(o) < \lambda, Y(t) < \lambda) - \mathbb{P}(Y(o) < \lambda, Y(t) < \lambda) \\ &= 1 - 2\mathbb{P}(Y(o) < \lambda) + \mathbb{P}(Y(o) < \lambda, Y(t) < \lambda). \end{aligned}$$

Since the random field $Y = \{Y(t), t \in \mathbb{R}^3\}$ is stationary, we can express $\mathbb{P}(Y(o) < \lambda)$ by means of the volume fraction p of the excursion set $\{t \in \mathbb{R}^3 : Y(t) > \lambda\}$, namely $\mathbb{P}(Y(o) < \lambda) = 1 - p$. Thus,

$$C(h) = 2p - 1 + \mathbb{P}(Y(o) < \lambda, Y(t) < \lambda). \tag{16}$$

Moreover, since the random vector $(Y(o), Y(t))$ follows the law of a bivariate χ^2_2-distribution, its (joint) probability distribution function is given by Equation (4.2) of [58]. Using this formula, we finally get that

$$\mathbb{P}(Y(o) < \lambda, Y(t) < \lambda) = (1 - \rho_X^2(h)) \sum_{j=0}^{\infty} \frac{\rho_X^{2j}(h)}{(j!)^2} \left(\int_0^{\frac{\lambda}{2(1-\rho_X^2(h))}} t^j \exp(-t) \mathrm{d}t \right)^2, \tag{17}$$

where $\rho_X : [0, \infty) \to [-1, 1]$ with $\rho_X(h) = \mathsf{Cov}(X(o), X(t))$ is the covariance function of the underlying Gaussian random field $X = \{X(t), t \in \mathbb{R}^3\}$. Plugging Equation (17) into Equation (16) completes the proof.

Appendix C: Representativity of image data and virtual structures

We provide additional information related to the representativity of the considered image data and the sampling window, used for generating the virtual nanostructures. First, we compute the standard deviation $\sigma_{\widehat{p}}$ of the volume fraction of the solid phase estimated from tomographic image data by means of the estimated two-point coverage probability function. Here we make use of Equation (6.83) in [6], which reads as

$$\sigma^2_{\widehat{p}} = \frac{1}{\nu(W)^2} \int_W \int_W C_0(|x - y|) \, \mathrm{d}x \, \mathrm{d}y,$$

where $\nu(W)$ denotes the volume of the observation window $W \subset \mathbb{R}^3$ and C_0 denotes the centered two-point coverage probability function. This can be simplified to

$$\sigma^2_{\widehat{p}} = \frac{1}{\nu(W)^2} \int_{\mathbb{R}^3} C_0(|x - y|) \, \nu((W - z) \cap W) \, \mathrm{d}z. \tag{18}$$

Plugging in the estimator $\widehat{C}_0$, which is directly obtained by the estimators $\widehat{C}$ and $\widehat{p}$, we compute an estimator for $\sigma_{\widehat{p}}$ for each sample. Here the integral in Equation (18) is approximated by a sum. The corresponding values are given in Table A2.

Table A2: Standard deviation $\sigma_{\widehat{p}}$ of the estimators for volume fractions of the solid phase computed via the two-point coverage probability function.

Sample	F850	F900	M850	M900	C850	C900
$\sigma_{\widehat{p}}$	$1.2 \cdot 10^{-3}$	$4.0 \cdot 10^{-3}$	$2.8 \cdot 10^{-3}$	$4.4 \cdot 10^{-3}$	$2.8 \cdot 10^{-3}$	$7.3 \cdot 10^{-3}$

Moreover, Table A3 shows the standard deviations of the estimators of all geometrical descriptors computed from 10 model realizations as discussed in Section 3.3. Note that the

standard deviations of both estimators for the volume fraction of the solid phase, computed from tomographic and simulated image data, are reasonably close to each other and that the standard deviations of the estimators of all remaining descriptors are at least one order of magnitude smaller than their mean values given in Table 2.

Table A3: Standard deviation of estimators for geometrical descriptors computed from simulated model realizations.

Sample	$\sigma_{\widehat{p}}$	$\sigma_{\widehat{S}/\mu\mathrm{m}^{-1}}$	$\sigma_{\widehat{\tau}_{\mathrm{geod}}}$ (solid)	$\sigma_{\widehat{\tau}_{\mathrm{geod}}}$ (pores)	$\sigma_{\widehat{\beta}}$ (solid)	$\sigma_{\widehat{\beta}}$ (pores)
F850 (sim)	$2.5 \cdot 10^{-3}$	$1.5 \cdot 10^{-2}$	$2.3 \cdot 10^{-3}$	$8.3 \cdot 10^{-4}$	$1.1 \cdot 10^{-2}$	$2.3 \cdot 10^{-3}$
F900 (sim)	$6.4 \cdot 10^{-3}$	$6.1 \cdot 10^{-2}$	$2.2 \cdot 10^{-3}$	$5.5 \cdot 10^{-3}$	$1.1 \cdot 10^{-2}$	$1.3 \cdot 10^{-2}$
M850 (sim)	$3.3 \cdot 10^{-3}$	$2.0 \cdot 10^{-2}$	$3.4 \cdot 10^{-3}$	$2.0 \cdot 10^{-3}$	$1.5 \cdot 10^{-2}$	$1.2 \cdot 10^{-2}$
M900 (sim)	$4.8 \cdot 10^{-3}$	$3.4 \cdot 10^{-2}$	$2.8 \cdot 10^{-3}$	$3.9 \cdot 10^{-3}$	$2.0 \cdot 10^{-2}$	$1.4 \cdot 10^{-2}$
C850 (sim)	$3.6 \cdot 10^{-3}$	$3.8 \cdot 10^{-2}$	$2.0 \cdot 10^{-3}$	$3.4 \cdot 10^{-3}$	$1.4 \cdot 10^{-2}$	$4.0 \cdot 10^{-3}$
C900 (sim)	$8.9 \cdot 10^{-3}$	$6.8 \cdot 10^{-2}$	$2.6 \cdot 10^{-3}$	$7.1 \cdot 10^{-3}$	$3.3 \cdot 10^{-2}$	$2.7 \cdot 10^{-2}$

References

[1] R. Golombek, A. Lind, H.-K. Ringkjøb, and P. Seljom. The role of transmission and energy storage in European decarbonization towards 2050. *Energy*, 239:122159, 2022.

[2] M. D. Radin, S. Hy, M. Sina, C. Fang, H. Liu, J. Vinckeviciute, M. Zhang, M. S. Whittingham, Y. S. Meng, and A. Van der Ven. Narrowing the gap between theoretical and practical capacities in Li-ion layered oxide cathode materials. *Advanced Energy Materials*, 7:1602888, 2017.

[3] Y. Zhao, X. Cao, G. Fang, Y. Wang, H. Yang, S. Liang, A. Pan, and G. Cao. Hierarchically carbon-coated $Na_3V_2(PO_4)_3$ nanoflakes for high-rate capability and ultralong cycle-life sodium ion batteries. *Chemical Engineering Journal*, 339:162–169, 2018.

[4] M. Müller, L. Schneider, N. Bohn, J. R. Binder, and W. Bauer. Effect of nanostructured and open-porous particle morphology on electrode processing and electrochemical performance of li-ion batteries. *ACS Applied Energy Materials*, 4(2):1993–2003, 2021.

[5] A. Wagner, N. Bohn, H. Geßwein, M. Neumann, M. Osenberg, A. Hilger, I. Manke, V. Schmidt, and J. R. Binder. Hierarchical structuring of NMC111-cathode materials in lithium-ion batteries: An in-depth study of the influence of primary and secondary particle size effects on electrochemical performance. *ACS Applied Energy Materials*, 3:12565–12574, 2020.

[6] S. N. Chiu, D. Stoyan, W. S. Kendall, and J. Mecke. *Stochastic Geometry and its Applications*. J. Wiley & Sons, Chichester, 3rd edition, 2013.

[7] D. Jeulin. *Morphological Models of Random Structures*. Springer, Cham, 2021.

[8] V. Schmidt, editor. *Stochastic Geometry, Spatial Statistics and Random Fields: Models and Algorithms*. Springer, Cham, 2015.

[9] B. Tjaden, D. J. L. Brett, and P. R. Shearing. Tortuosity in electrochemical devices: a review of calculation approaches. *International Materials Reviews*, 63:47–67, 2018.

[10] S. R. Kalidindi, M. Buzzy, B. L. Boyce, and R. Dingreville. Digital twins for materials. *Frontiers in Materials*, 9:48, 2022.

[11] B. Prifling, D. Westhoff, V. Schmidt, H. Markötter, I. Manke, V. Knoblauch, and V. Schmidt. Parametric microstructure modeling of compressed cathode materials for Li-ion batteries. *Computational Materials Science*, 169:109083, 2019.

[12] D. Westhoff, J. Feinauer, K. Kuchler, T. Mitsch, I. Manke, S. Hein, A. Latz, and V. Schmidt. Parametric stochastic 3D model for the microstructure of anodes in lithium-ion power cells. *Computational Materials Science*, 126:453–467, 2017.

[13] D. Westhoff, I. Manke, and V. Schmidt. Generation of virtual lithium-ion battery electrode microstructures based on spatial stochastic modeling. *Computational Materials Science*, 151:53–64, 2018.

[14] O. Furat, L. Petrich, D. P. Finegan, D. Diercks, F. Usseglio-Viretta, K. Smith, and V. Schmidt. Artificial generation of representative single Li-ion electrode particle architectures from microscopy data. *npj Computational Materials*, 7:105, 2021.

[15] A. Gayon-Lombardo, L. Mosser, N. P. Brandon, and S. J. Cooper. Pores for thought: generative adversarial networks for stochastic reconstruction of 3D multi-phase electrode microstructures with periodic boundaries. *npj Computational Materials*, 6:82, 2020.

[16] S. Kamrava and H. Mirzaee. End-to-end three-dimensional designing of complex disordered materials from limited data using machine learning. *Physical Review E*, 106:055301, 2022.

[17] H. Xu, J. Zhu, D. P. Finegan, H. Zhao, X. Lu, W. Li, N. Hoffman, A. Bertei, P. Shearing, and M. Z. Bazant. Guiding the design of heterogeneous electrode microstructures

for Li-ion batteries: microscopic imaging, predictive modeling, and machine learning. *Advanced Energy Materials*, 11:2003908, 2021.

[18] B. Prifling, M. Ademmer, F. Single, O. Benevolenski, A. Hilger, M. Osenberg, Ingo Manke, and V. Schmidt. Stochastic 3D microstructure modeling of anodes in lithium-ion batteries with a particular focus on local heterogeneity. *Computational Materials Science*, 192:110354, 2021.

[19] B. Abdallah, F. Willot, and D. Jeulin. Morphological modelling of three-phase microstructures of anode layers using SEM images. *Journal of Microscopy*, 263:51–63, 2016.

[20] H. Moussaoui, J. Laurencin, Y. Gavet, G. Delette, M. Hubert, P. Cloetens, T. Le Bihan, and J. Debayle. Stochastic geometrical modeling of solid oxide cells electrodes validated on 3D reconstructions. *Computational Materials Science*, 143:262–276, 2018.

[21] H. Moussaoui, R. K. Sharma, J. Debayle, Y. Gavet, G. Delette, and J. Laurencin. Microstructural correlations for specific surface area and triple phase boundary length for composite electrodes of solid oxide cells. *Journal of Power Sources*, 412:736–748, 2019.

[22] M. Neumann, C. Hirsch, J. Staněk, V. Beneš, and V. Schmidt. Estimation of geodesic tortuosity and constrictivity in stationary random closed sets. *Scandinavian Journal of Statistics*, 46:848–884, 2019.

[23] M. Neumann, M. Osenberg, A. Hilger, D. Franzen, T. Turek, I. Manke, and V. Schmidt. On a pluri-gaussian model for three-phase microstructures, with applications to 3D image data of gas-diffusion electrodes. *Computational Materials Science*, 156:325–331, 2019.

[24] L. Holzer and M. Cantoni. Review of FIB-tomography. In I. Utke, S. Moshkalev, and P. Russell, editors, *Nanofabrication using Focused Ion and Electron Beams: Principles and Applications*, pages 410–435. Oxford University Press: New York, 2012.

[25] G. Möbus and B. J. Inkson. Nanoscale tomography in materials science. *Materials Today*, 10:18–25, 2007.

[26] D. Zhang, A. Bertei, F. Tariq, N. Brandon, and Q. Cai. Progress in 3D electrode microstructure modelling for fuel cells and batteries: transport and electrochemical performance. *Progress in Energy*, 1:012003, 2019.

[27] A. Lang and C. Schwab. Isotropic Gaussian random fields on the sphere: regularity, fast simulation and stochastic partial differential equations. *The Annals of Applied Probability*, 25:3047–3094, 2015.

[28] D. Marinucci and G. Peccati. *Random Fields on the Sphere: Representation, Limit Theorems and Cosmological Applications*. Cambridge University Press, Cambridge, 2011.

[29] J. Feinauer, A. Spettl, I. Manke, S. Strege, A. Kwade, A. Pott, and V. Schmidt. Structural characterization of particle systems using spherical harmonics. *Materials Characterization*, 106:123–133, 2015.

[30] M. Neumann, O. Stenzel, F. Willot, L. Holzer, and V. Schmidt. Quantifying the influence of microstructure on effective conductivity and permeability: virtual materials testing. *International Journal of Solid and Structures*, 184:211–220, 2020.

[31] B. Prifling, M. Röding, P. Townsend, M. Neumann, and V. Schmidt. Large-scale statistical learning for mass transport prediction in porous materials using 90,000 artificially generated microstructures. *Frontiers in Materials*, 8:786502, 2021.

[32] B. Prifling, M. Weber, N. Ray, A. Prechtel, M. Phalempin, S. Schlüter, D. Vetterlein, and V. Schmidt. Quantifying the impact of 3D pore space morphology on soil gas diffusion in loam and sand. *Transport in Porous Media*, 2023. (in print).

[33] O. Stenzel, O. M. Pecho, L. Holzer, M. Neumann, and V. Schmidt. Predicting effective conductivities based on geometric microstructure characteristics. *AIChE Journal*, 62:1834–1843, 2016.

[34] N. Otsu. A threshold selection method from gray-level histograms. *IEEE Transactions on Systems, Man, and Cybernetics*, 9:62–66, 1979.

[35] M. Osenberg, A. Hilger, M. Neumann, A. Wagner, N. Bohn, J. R. Binder, V. Schmidt, J. Banhart, and I. Manke. Classification of FIB/SEM-tomography images for highly porous multiphase materials using random forest classifiers. *Journal of Power Sources*, 570:233030, 2023.

[36] J. Schindelin, I. Arganda-Carreras, E. Frise, V. Kaynig, M. Longair, T. Pietzsch, S. Preibisch, C. Rueden, S. Saalfeld, B. Schmid, J.-Y. Tinevez, D. W. White, V. Hartenstein, K. Eliceiri, P. Tomancak, and A. Cardona. Fiji: an open-source platform for biological-image analysis. *Nature Methods*, 9:676, 2012.

[37] A. Spettl, R. Wimmer, T. Werz, M. Heinze, S. Odenbach, C. E. Krill III, and V. Schmidt. Stochastic 3D modeling of Ostwald ripening at ultra-high volume fractions of the coarsening phase. *Modelling and Simulation in Materials Science and Engineering*, 23:065001, 2015.

[38] E. J. Garboczi and J. W. Bullard. 3D analytical mathematical models of random star-shape particles via a combination of X-ray computed microtomography and spherical harmonic analysis. *Advanced Powder Technology*, 28:325–339, 2017.

[39] R. J. Adler and J. E. Taylor. *Random Fields and Geometry*. Springer, New York, 2009.

[40] Y. L. Tong. *Probability Inequalities in Multivariate Distributions*. Academic Press, New York, 1980.

[41] J. Ohser and K. Schladitz. *3D Images of Materials Structures: Processing and Analysis*. Wiley-VCH, Weinheim, 2009.

[42] L. Holzer, P. Marmet, M. Fingerle, A. Wiegmann, M. Neumann, and V. Schmidt. *Tortuosity and Microstructure Effects in Porous Media: Classical Theories, Empirical Data and Modern Methods*. Springer, Cham, 2023.

[43] L. Holzer, D. Wiedenmann, B. Münch, L. Keller, M. Prestat, P. Gasser, I. Robertson, and B. Grobéty. The influence of constrictivity on the effective transport properties of porous layers in electrolysis and fuel cells. *Journal of Materials Science*, 48:2934–2952, 2013.

[44] J. Zahnow, T. Bernges, A. Wagner, N. Bohn, J. R. Binder, W. G. Zeier, M. T. Elm, and J. Janek Impedance analysis of NCM cathode materials: electronic and ionic partial conductivities and the influence of microstructure. *ACS Applied Energy Materials*, 4:1335–1345, 2021.

[45] D. Hlushkou, H. Liasneuski, U. Tallarek, and S. Torquato. Effective diffusion coefficients in random packings of polydisperse hard spheres from two-point and three-point correlation functions. *Journal of Applied Physics*, 118:124901, 2015.

[46] J. Joos, T. Carraro, M. Ender, B. Rüger, A. Weber, and E. Ivers-Tiffée. Detailed microstructure analysis and 3D simulations of porous electrodes. *ECS Transactions*, 35:2357, 2011.

[47] F. Willot, B. Abdallah, and Y.-P. Pellegrini. Fourier-based schemes with modified green operator for computing the electrical response of heterogeneous media with accurate local fields. *International Journal for Numerical Methods in Engineering*, 98:518–533, 2014.

[48] T. Carraro, S. E. Wetterauer, A. V. Ponce-Bobadilla, and D. Trucu. A level-set approach for a multi-scale cancer invasion model. *Mathematics in Applied Sciences and Engineering*, 2:1–71, 2021.

[49] M. Landstorfer, B. Prifling, and V. Schmidt. Mesh generation for periodic 3D microstructure models and computation of effective properties. *Journal of Computational Physics*, 431:110071, 2021.

[50] J. Newman and W. Tiedemann. Porous-electrode theory with battery applications. *AIChE Journal*, 21:25–41, 1975.

[51] M. Neumann, O. Furat, D. Hlushkou, U. Tallarek, L. Holzer, and V. Schmidt. On microstructure-property relationships derived by virtual materials testing with an emphasis on effective conductivity. In M. Baum, G. Brenner, J. Grabowski, T. Hanschke, S. Hartmann, and A. Schöbel, editors, *Simulation Science: First International Workshop, SimScience 2017, Göttingen, Germany, April 27-28, 2017, Revised Selected Papers*, pages 145–158. Springer, Communications in Computer and Information Science (CIS), Berlin, 2018.

[52] S. Hein, T. Danner, D. Westhoff, B. Prifling, R. Scurtu, L. Kremer, A. Hoffmann, A. Hilger, M. Osenberg, I. Manke, M. Wohlfahrt-Mehrens, V. Schmidt, and A. Latz. Influence of conductive additives and binder on the impedance of lithium-ion battery electrodes: effect of morphology. *Journal of The Electrochemical Society*, 167:013546, 2020.

[53] B. Prifling, M. Neumann, S. Hein, T. Danner, E. Heider, A. Hoffmann, P. Rieder, A. Hilger, M. Osenberg, I. Manke, M. Wohlfahrt-Mehrens, A. Latz, and V. Schmidt. Quantitative comparison of different approaches for reconstructing the carbon-binder

domain from tomographic image data of cathodes in lithium-ion batteries and its influence on electrochemical properties. *Energy Technology*, 10:2200784, 2022.

[54] T. Danner, G. Zhu, A. F. Hofmann, and A. Latz. Modeling of nano-structured cathodes for improved lithium-sulfur batteries. *Electrochimica Acta*, 184:124–133, 2015.

[55] A. Schmidt, E. Ramani, T. Carraro, J. Joos, A. Weber, M. Kamlah, and E. Ivers-Tiffée. Understanding deviations between spatially resolved and homogenized cathode models of lithium-ion batteries. *Energy Technology*, 9:2000881, 2021.

[56] M. Doyle, T. F. Fuller, and J. Newman. Modeling of galvanostatic charge and discharge of the lithium/polymer/insertion cell. *Journal of The Electrochemical Society*, 140(6), 1993.

[57] S. Lueth, U. S. Sauter, and W. G. Bessler. An agglomerate model of lithium-ion battery cathodes. *Journal of The Electrochemical Society*, 163(2):A210, 2015.

[58] R. F. Gunst and J. T. Webster. Density functions of the bivariate chi-square distribution. *Journal of Statistical Computation and Simulation*, 2:275–288, 1973.